# Early experience in the use of quantitative image quality measurements for the quality assurance of full field digital mammography x-ray systems

**N W Marshall**

Clinical Physics Group, Barts and the London NHS Trust, St Bartholomew's Hospital,
London EC1A 6BE, UK

**Abstract**

Quantitative image quality results in the form of the modulation transfer function (MTF), normalized noise power spectrum (NNPS) and detective quantum efficiency (DQE) are presented for nine full field digital mammography (FFDM) systems. These parameters are routinely measured as part of the quality assurance (QA) programme for the seven FFDM units covered by our centre. Just one additional image is required compared to the standard FFDM protocol; this is the image of an edge, from which the MTF is calculated. A variance image is formed from one of the flood images used to measure the detector response and this provides useful information on the condition of the detector with respect to artefacts. Finally, the NNPS is calculated from the flood image acquired at a target detector air kerma (DAK) of 100 $\mu$Gy. DQE is then estimated from these data; however, no correction is currently made for effects of detector cover transmission on DQE. The coefficient of variation ($cov$) of the 50% point of the MTF for five successive MTF results was 1%, while the $cov$ for the 50% MTF point for an $a$-Se system over a period of 17 months was approximately 3%. For four $a$-Se based systems, the $cov$ for the NNPS at 1 mm$^{-1}$ for a target DAK of 100 $\mu$Gy was approximately 4%; the same result was found for four CsI based FFDM units. With regard to the stability of NNPS over time, the $cov$ for four NNPS results acquired over a period of 12 months was also approximately 4%. The effect of acquisition geometry on NNPS was also assessed for a CsI based system. NNPS data acquired with the antiscatter grid in place showed increased noise at low spatial frequency; this effect was more severe as DAK increased. DQE results for the three detector types ($a$-Se, CsI and CR) are presented as a function of DAK. Some reduction in DQE was found for both the $a$-Se and CsI based systems at a target DAK of 12.5 $\mu$Gy when compared to DQE data acquired at 100 $\mu$Gy. For the CsI based systems, DQE at 1 mm$^{-1}$ fell from 0.49 at 100 $\mu$Gy to 0.38 at 12.5 $\mu$Gy. For the $a$-Se units, there was a slightly greater reduction in average DQE at 1 mm$^{-1}$, from 0.53 at 100 $\mu$Gy to 0.31 at 12.5 $\mu$Gy. Somewhat different behaviour was seen for the CR unit; DQE

(at 1 mm$^{-1}$) increased from 0.40 at 100 $\mu$Gy to 0.49 at 12.5 $\mu$Gy; however, DQE fell to 0.30 at 420 $\mu$Gy. DQE stability over time was assessed using the *cov* of DQE at 1 mm$^{-1}$ and a target DAK of 100 $\mu$Gy; the *cov* for data acquired over a period of 17 months for an *a*-Se system was approximately 7%. For comparison with conventional testing methods, the *cov* was calculated for contrast-detail (cd) data acquired over the same period of time for this unit. The *cov* for the threshold contrast results (averaged for disc diameters between 0.1 mm and 2 mm) was 6%, indicating similar stability.

## 1. Introduction

Full field digital mammography (FFDM) systems are used for both breast screening and assessment at Barts and the London NHS Trust. Three FFDM system types are used for this purpose; the GE Senographe DS, the Hologic Selenia and the Agfa Embrace DM1000. With regard to routine quality assurance (QA), these units are assessed at six monthly intervals according to standard protocols at the UK and European level (IPEM 2005a, 2005b, EC 2006, NHSBSP 2006). Image quality assessment in these protocols is based on the use of semi-quantitative test objects such as the CDMAM contrast-detail (cd) test object; in fact current European (and UK) standards for FFDM systems are framed using this test object (EC 2006, NHSBSP 2006). Other test objects, such as TOR(MAM), are also used as they offer a quick and reasonably sensitive routine check on image quality (NHSBSP 2006).

As an adjunct to these test object methods, the use of quantitative methods has been developed for image quality assessment as part of the routine QA of these systems. Parameters measured include the pre-sampling modulation transfer function (MTF), normalized noise power spectrum (NNPS) and the detective quantum efficiency (DQE). These methods are well established (Metz *et al* 1995) and have been successfully applied to the evaluation of x-ray detectors in computed radiography (CR) systems (Workman and Cowen 1993, Samei and Flynn 2002), fluoroscopy systems (Tapiovaara 1993), direct and indirect digital radiography systems (Samei and Flynn 2003) and small field digital mammography systems (Evans *et al* 2002). Bloomquist *et al* (2006) and Yaffe *et al* (2006) have described the use of MTF and noise power spectrum (NPS) within the ACRIN DMIST trial. Yaffe *et al* (2006) conclude that the MTF is a useful measure and should be measured annually; however, they also state that the routine measurement of NPS was thought to be of limited use, due in part to difficulties in normalizing signals between systems. While these papers provide extremely useful data with regard to the set up of QA programmes for FFDM systems, only limited information on the measurement of MTF and NPS is given for these units.

In previous work, quantitative measurements have been compared with subjective (cd) image quality results for an FFDM system (Marshall 2006a) and the utility of quantitative image quality parameters when diagnosing detector problems has been demonstrated (Marshall 2006b). The aim of this paper is to extend this work to a range of systems and examine differences in these parameters for a number of FFDM units of the same type, as well as for different FFDM technologies, using an identical method. The work will also examine the stability of these parameters over time, the ease with which they might be included in a routine QA programme and discuss some of the problems encountered during the implementation. It should be noted that the data presented in the coming sections are what might be termed 'field' results, aimed at physicists performing routine QA measurements, rather than painstaking laboratory grade results.

**Table 1.** Technical parameters for the FFDM systems assessed.

| System | Detector | Approx image size (cm) | Matrix size | Pixel size[a] (mm) |
|---|---|---|---|---|
| Hologic Selenia | $a$-Se/TFT | $24 \times 29$ | $3420 \times 4096$ | 0.07 |
| Agfa DM 1000 | $a$-Se/TFT | $24 \times 29$ | $3420 \times 4096$ | 0.07 |
| GE Senographe DS | CsI/TFT | $19 \times 23$ | $1914 \times 2294$ | 0.094 |
| Konica CR | CR plate | $24 \times 30$ | $5580 \times 6980$ | 0.043 |

[a] Pixel size is taken from Dicom tag (0018,1164) 'Imager Pixel Spacing'.

## 2. Materials and methods

### 2.1. The FFDM systems studied

This study presents data for nine FFDM systems; four GE Senographe DS units, three Hologic Selenia systems, an Agfa Embrace DM1000 and a Konica computed radiography (CR) unit. The Agfa unit is based closely on the Hologic Selenia system. Routine quantitative measurements are made for two Hologic Selenia, the Agfa DM1000 and the four GE Senographe systems. The second Hologic Selenia system and the Konica CR system were assessed as part of a one-off visit to two separate sites, external to this NHS Trust. Details of the FFDM systems are presented in table 1. FFDM systems that utilize direct conversion ($a$-Se x-ray converter), indirect conversion (CsI) and photostimulable phosphor plate x-ray detectors are therefore compared in this study.

For the units within this NHS Trust, the data required to calculate the quantitative parameters are acquired during the routine (six monthly) QA visit. Little additional time is required to acquire these image data; NNPS is calculated from the uniform x-ray (flood) images that are used in the measurement of the detector response function (EC 2006, NHSBSP 2006), also termed the signal transfer property (STP). MTF is calculated from one image of an edge test object acquired after the flood images. These image data are either saved onto CD-R during the QA visit or transferred to a radiological work station (RWS) and then burnt onto CD-R at the end of the QA survey.

### 2.2. X-ray factors used for image acquisition

In order to increase the efficiency of QA tests, the same factors should be used when measuring the STP and the NNPS, as this removes repeated image acquisitions under different beam conditions. Both of these parameters can be calculated from the same set of flood images. The UK FFDM protocol states that the STP should be measured using the clinical x-ray factors selected under automatic exposure control (AEC) for 4.5 cm polymethylmethacralate (PMMA). However, varying the acquisition factors according to AEC selection across the different units would add additional variation at what is a relatively early stage in the use of quantitative image quality measurements. Furthermore, when this study began the available International Electrotechnical Commission (IEC) draft for the standard mammography beam recommended the use of 4 cm PMMA for NPS estimation (although this has now changed and the current IEC standard recommends the use of 2 mm Al). NNPS data were therefore acquired using an x-ray spectrum of 28 kV, Mo/Mo target filter combination and 4 cm added PMMA suspended at the x-ray tube exit port. Note that the anti-scatter grid is routinely removed for this measurement to enable an accurate estimate of air kerma at the detector entrance plane; the effect of the grid on the NNPS was investigated for one system.

With regard to MTF measurement, results are presented for several beam qualities and geometries. These include MTF measured with and without 4 cm PMMA in the x-ray beam and edge placed directly on the detector compared to edge placed on the breast support platform. The effect of added Al filtration on MTF was also studied. Strictly, the NNPS and the MTF should be acquired under identical beam conditions; however, the presence of PMMA introduces considerable quantities of scattered radiation in to the MTF result (the new IEC standard using 2 mm Al avoids this problem). Comparison of MTF across units was performed without additional x-ray beam filtration (i.e. without the 4 cm added PMMA in the x-ray beam).

### 2.3. System acquisition settings

Images used in the analysis for the $a$-Se types (Hologic Selenia and Agfa DM1000) were acquired as 'Flat field'; these images have a linear relationship between pixel value (PV) detector air kerma (DAK) and minimal image processing. Quantitative image quality data were calculated from 'RAW' images for the GE Senographe units, with the proprietary 'FineView' and 'PremiumView' processing disabled. Settings for the Konica system were 'Fix' readout mode, 'QC $S$-value' with 'E' and 'F' processing turned off. When acquiring successive images for NPS estimation a 60 s delay was maintained between exposures for all units.

### 2.4. The signal transfer property (STP)

The signal transfer property is measured as part of the current QA protocol as follows. The additional 4 cm of PMMA is suspended in the compression plate as close to the x-ray tube exit port as the system will allow. This is considered to be a safer option than simply taping the PMMA blocks to the x-ray tube. The detector is then covered using a Pb beam block and a calibrated dosemeter is placed at a known distance (8 cm) above the breast support platform. The tube current–time product (mAs) is then varied between 10 mAs and 160 mAs, and the air kerma per unit mAs at the detector entrance plane is calculated from these output measurements, the chamber calibration factor and the inverse square correction. Output linearity with changing mAs is routinely assessed as part of the tube and generator tests; all systems show good linearity with mAs.

The ionization chamber and Pb protection are then removed. For both the Hologic Selenia and Agfa DM1000 units, the grid is retracted internally and therefore the detector remains protected by the carbon fibre cover of the breast support platform. With the GE Senographe systems, the grid is removed by removing the entire table bucky, leaving the detector exposed (covered by what appears to be a dark grey carbon-like material). For the Konica CR system, the plates were exposed placed on top of the breast support platform. No correction was attempted between systems for the different detector covers or CR cassette window entrance. Inevitably, this leads to increased error/uncertainty when estimating air kerma at the detector entrance plane—an uncertainty that feeds through to the DQE estimate.

Target DAK for the NNPS (and hence DQE) measurement is an important consideration as DQE can vary with detector entrance air kerma (Illers *et al* 2004a). Data should be acquired at a DAK that reflects the typical operating DAK for these systems. When the study was initiated, average DAK values for the $a$-Se units and the Senographe units taken from early routine QA data were approximately 95 $\mu$Gy and 100 $\mu$Gy, respectively, for imaging 4.5 cm PMMA. These values reflect the initial DAK chosen by the system design engineers, along with input from the manufacturer's application specialists. Target DAK values of 12.5, 25,

50, 100, 200 and 400 $\mu$Gy were therefore chosen for the flood images. The mAs settings required to give these DAK values were calculated from the output measurements detailed above. Actual mAs settings used occasionally differed from the required setting as there is a limited range of dial mAs values available on most systems. The output results used to establish the STP and the STP itself were also assessed over time, in order to test the stability and long-term reproducibility of these methods.

The STP is used to normalize and linearize the images before calculating MTF and NNPS. This can be found by plotting PV versus the number of photons at the detector (Illers *et al* 2004a) as described in the IEC method (IEC 2004) or by plotting PV against DAK. The IEC conversion method was used previously (Marshall 2006b); however, an STP found by plotting PV versus DAK is now used. This process converts PV in the original image to air kerma; the mean value of a linearized image should be equal to the air kerma at which the image was acquired. For example, the CR system has a logarithmic response:

$$PV = A + B \ln(K_a) \tag{1a}$$

where $K_a$ is the air kerma. Linearized images ($I_{\text{lin}}(x_i, y_j)$) were formed from the original greyscale image (PV in $I_{\text{input}}(x_i, y_j)$) using the following equation:

$$I_{\text{lin}}(x_i, y_j) = \exp((I_{\text{input}}(x_i, y_j) - A)/B). \tag{1b}$$

### 2.5. The modulation transfer function (MTF)

The MTF is measured using the edge technique (Cunningham and Reid 1992, Samei *et al* 1998, Carton *et al* 2005). The details of our implementation are given elsewhere (Marshall 2006a); however, the relevant points are presented briefly here. It should be noted that a 1 mm steel plate of dimensions 10 cm $\times$ 10 cm is now used instead of the 0.5 mm Cu plate used previously. All four sides of this plate have been machined to a straight edge. The steel plate is placed on the breast support platform and twisted to give a slight angle between the straight edge and the pixel matrix—typically between 1° and 5°. The edge was imaged on the table top with the anti-scatter grid in place so that a consistent geometry could be used between the different systems. The following naming conventions are used for spatial frequency directions; $u$ indicates data for the chest-wall to the nipple direction while $v$ indicates results for the left–right direction across the detector.

A region of interest (ROI) was used to extract a 5 cm $\times$ 5 cm section of image with the edge roughly at the centre. The angle of the edge was then determined using a simple linear least squares fit and the 2D image data were re-projected around the angled edge (Samei *et al* 1998) to form an edge spread function (ESF) with a bin spacing of 0.1 pixels. The ESF was smoothed with a median filter of five bins and then the ESF was differentiated to obtain the line spread function (LSF). Finally, the LSF is Fourier transformed to give the pre-sampling MTF. Note that the MTF is calculated for the two different detector directions from just one edge image. Horizontal and vertical MTFs are therefore extracted from different detector regions—this was considered acceptable for field/QA conditions as both MTFs can be acquired from a single image. Time to acquire the edge image and calculate and import the MTFs into the QA database using this method is roughly 5 min. Short-term reproducibility for this method was assessed by acquiring five successive edge images on a Senographe DS system. The edge was removed and replaced on to the breast support table and a 1 min gap was left between exposures.

## 2.6. Variance image (VI)

A greyscale image can be formed of the variance present in the flood images prior to NPS estimation (Maidment *et al* 2003, Marshall 2006a). This technique has proved useful in quickly identifying artefacts that can be difficult to find in large greyscale images. Details of the method used to calculate a VI are given elsewhere (Marshall 2006a). To emphasize the utility of this method, further VI examples are presented here.

## 2.7. Normalized noise power spectrum (NNPS)

The NNPS data are calculated from the STP images using a standard 2D NNPS algorithm; full details are given elsewhere (Marshall 2006a). Briefly, a sub-image is first extracted from the flood image and linearized as described in the STP section. For the $a$-Se and Senographe units, a sub-image of $1088 \times 1088$ pixels was used and this corresponds to physical dimensions of $7.6 \times 7.6$ cm and $10.8 \times 10.8$ cm, respectively. The pixel size of the CR system studied was only 0.043 mm and therefore a sub-image of $2176 \times 2176$ pixels was used, corresponding to a region of 9.4 cm $\times$ 9.4 cm. Half overlapping ROIs (IEC 2004) of size $128 \times 128$ pixels for the $a$-Se and Senographe units and $256 \times 256$ pixels for the CR system, were then taken from the sub-image. A total of 128 ROIs are taken from each flood image. A 2D second-order polynomial was then used to correct each ROI for low-frequency background effects that may be present in the image. The squared modulus of the 2D fast Fourier transform (FFT) of each ROI was calculated and added to the NPS ensemble. This was repeated for all the ROIs taken from each image. Finally, the NNPS is calculated by dividing the ensemble by the square mean value of the sub-image i.e. by (air kerma)$^2$.

The spectra are then sectioned along the $u$ and $v$ spatial frequency axes; five spatial frequency bins on either side of the axes are used in the NNPS binning. The axes themselves ($u = 0$ and $v = 0$) are excluded from the NPS as low-frequency artefacts, from the heel effect for example, often appear in these bins (Dobbins 2000), although some authors include these values (Samei and Flynn 2002). A greyscale image of the NNPS ensemble is also formed as this gives a visual impression of the full 2D NNPS.

Routinely, QA noise power spectra are calculated from just one image. The relative uncertainty can be calculated as $1/\sqrt{N_{bin}}$, where $N_{bin}$ is the number of independent frequency bin results associated with a given NPS value (Dobbins *et al* 2006). $N_{bin}$ is calculated as follows:

$$N_{bin} = M \text{ rows bin}_{ave} \tag{2}$$

where $M$ is the number of ROIs (spectra), 'rows' is the number of rows used to section the NPS and bin$_{ave}$ is the average number of NPS points in a bin per row. As an example, a noise power spectrum for an $a$-Se unit using $128 \times 128$ pixel ROIs from one image has a frequency resolution ($\Delta f$) of 0.11 mm$^{-1}$. For the case of non-overlapping ROIs with no spatial frequency re-binning, $N_{bin} = 64 \times 10 \times 1$ and the spectral uncertainty is $\sim 4\%$. Re-binning spatial frequencies into 0.5 mm$^{-1}$ bins would give bin$_{ave} = 4.48$ and reduce spectral uncertainty to $\sim 1.8\%$, at the expense of spatial resolution. Changing to half-overlapping spectra complicates the calculation of uncertainty (Dobbins *et al* 2006) but for spectra calculated without windowing (as is the case here), the uncertainty is reduced by the square root of the reciprocal of the number of independent pixels between the two cases. Therefore, the uncertainty for a power spectrum taken from just one image is reduced to approximately 3.7%. Spectral data are routinely calculated from one or two images with no re-binning using half-overlapping ROIs, giving a typical uncertainty of between 3.7% and 2.6%.

## 2.8. Detective quantum efficiency (DQE)

DQE was calculated from the pre-sampling MTF and NNPS using the following equation:

$$\mathrm{DQE}(u, v) = \frac{\mathrm{MTF}^2(u, v)}{K_a \; \mathrm{SNR}^2_{\mathrm{in}} \cdot \mathrm{NNPS}(u, v)} \tag{3}$$

where $K_a$ is the air kerma for the particular NNPS result and $\mathrm{SNR}^2_{\mathrm{in}}$ is the number of photons per unit $\mu$Gy per mm$^2$. A value of 5300 photons $\mu\mathrm{Gy}^{-1}$ mm$^{-2}$ is used in these calculations for all systems in this paper in order to remain consistent with previous work (Marshall 2006a). From the range of measured half value layer data (HVL) for seven of these systems, it is estimated that differences in intrinsic x-ray filtration will lead to a maximum difference of 1.4% in the number of photons $\mu\mathrm{Gy}^{-1}$ mm$^{-2}$. Compression plate thickness and composition will also have a small effect on this number.

## 2.9. Link to contrast-detail results

Quantitative measurements offer a somewhat abstract description of image detector image quality compared to a typical image quality metric such the threshold cd curve that is often used to frame image quality standards (Hay *et al* 1985, IPEM 2005b, EC 2006). Several authors have examined the relationship between quantitative measurements such as DQE and cd performance (Aufrichtig 1999, Aufrichtig and Xue 2000, Marshall 2006a, Borasi *et al* 2006). Linking cd performance to the underlying quantitative detector data is an important step in the acceptance of quantitative measurements as part of a QA programme. Although not the explicit aim of this paper, this section gives a brief comparison of cd results and the quantitative detector measurements.

For this purpose, cd data were acquired using the CDMAM cd test object (manufactured by Artinis Medical Systems B.V., The Netherlands) for one *a*-Se (Selenia_1) system, one CsI (Seno_3) system and for the Konica CR system. Acquisition factors were a DAK of 100 $\mu$Gy, 28 kV and a Mo/Mo target/filter combination. Two cd images were acquired at these settings and these were scored by one experienced observer. Ideally, the images from the three different systems would be scored using the same softcopy workstation (SCW); however, this was not possible. For the *a*-Se and CsI units, the system default SCW was used; these are five megapixel cathode ray tube (CRT) units. The CR images were transferred to a remote SCW and scored using a pair of five megapixel TFT displays. Luminance response for all these displays is checked using a luminance meter as part of the routine SCW quality assurance checks. It is therefore assumed that the displays have been well set up and are not the determining factor in the observer scoring of the cd images. During cd scoring, ambient light was kept low and screen reflections were kept to a minimum. Window level, width and software magnification were adjusted by the observer to maximize visibility of cd details. The CDMAM scoring method was followed (as described in the CDMAM manual); once the number of discs at each detail size has been established, the gold thickness of the last visible disc is converted into a contrast (EC 2006). This threshold contrast is then plotted against detail diameter on a log–log graph and a second-order quadratic function fitted to the cd results (Marshall 2006a, Borasi *et al* 2006).

The cd response expected from the quantitative results was calculated using a matched filter SNR from signal detection theory (Wagner and Brown 1985, Aufrichtig 1999); the steps required are detailed elsewhere (Marshall 2006a). Following Workman and Cowen (1993), it was assumed that the observers minimize the effect of visual bias on the cd result and therefore an ideal visual response function was used in these calculations. Furthermore, no allowance
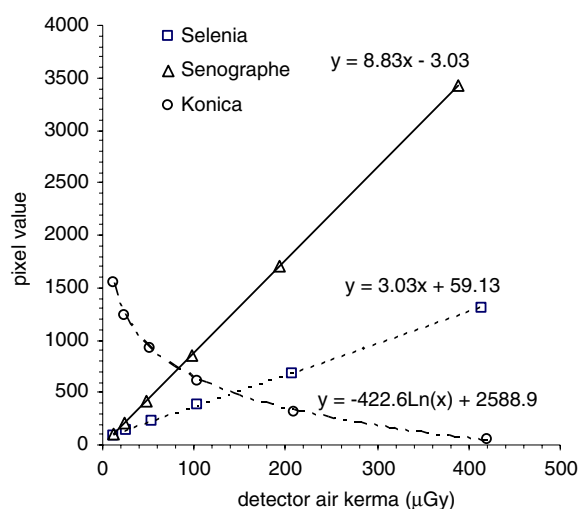
**Figure 1.** Example STP curves for two systems with linear response (Selenia and Senographe) and logarithmic response (Konica CR system).

**Table 2.** STP results for nine different systems at 28 kV Mo/Mo and 4 cm added Perspex ($A$ and $B$ are coefficients in $PV_{lin} = A + B(K_a)$ for linear systems and $PV_{log} = A + B \ln(K_a)$ for the Konica CR system).

| Coefficient | Selenia_1 | Selenia_2 | Selenia_3 | Agfa | Seno_1 | Seno_2 | Seno_3 | Seno_4 | Konica |
|---|---|---|---|---|---|---|---|---|---|
| $A$ | 59.1 | 59.4 | 65.4 | 54.8 | −3.0 | −1.8 | −1.9 | 1.3 | 2588.9 |
| $B$ | 3.03 | 3.39 | 3.36 | 3.76 | 8.83 | 8.27 | 8.96 | 8.80 | −422.6 |

has been made for any differences in system grid performance that may be present between the three different x-ray systems on the imaged contrasts of the discs.

## 3. Results and discussion

### 3.1. STP

Figure 1 shows example STP curves for the $a$-Se and the CsI based units (both have a linear relationship between PV and DAK) and for the Konica CR system (which has a logarithmic relationship). The *cov* for output measured with 4 cm Perspex in the x-ray beam (over a period of 17 months) was between 1% and 2% for Selenia and Senographe units, indicating similar stability to that found for the standard specific radiation output for routine QA tests. Table 2 shows STP results for the entire range of systems assessed. As expected, STP coefficients are similar for the Senographe units. There is also little difference in the coefficients between the $a$-Se based units (three Hologic systems and one Agfa system), indicating similar calibration for these systems. The STP gradient is probably not expected to remain unchanged over the detector lifetime due to changes in gain and routine or ad hoc recalibration of the detector by the service engineer. However, *cov* for the $B$ coefficient of the STP (i.e. the gradient) for one example $a$-Se unit is quite stable over a period of 17 months (12%) although this does include one entire system re-configuration; *cov* for the Senographe system is approximately 6% (table 3).
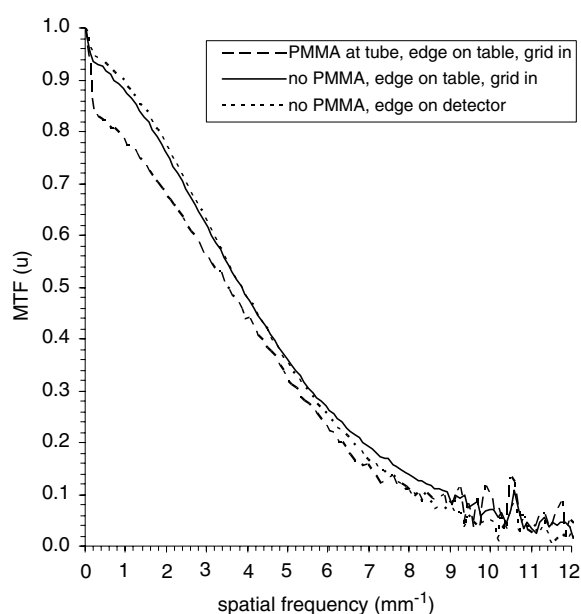
**Figure 2.** Effect of geometry on the MTF for a CsI based system (*u* direction).

**Table 3.** Stability of STP results over time for a Selenia and a Senographe system over time.

| | Selenia | | | Senographe | |
|---|---|---|---|---|---|
| Date | *A* | *B* | Date | *A* | *B* |
| Feb-05 | 53.0 | 3.04 | Oct-04 | 9.0 | 9.63 |
| Aug-05 | 80.2 | 3.02 | Apr-05 | 6.0 | 8.47 |
| Dec-05 | 58.9 | 3.05 | Oct-05 | −2.0 | 8.28 |
| Mar-06 | 59.2 | 3.03 | Mar-06 | −1.8 | 8.28 |
| Jul-06 | 63.1[a] | 3.98[a] | Sep-06 | −0.8 | 8.67 |

[a] Detector re-calibrated.

## 3.2. MTF

Reproducibility of the MTF was assessed from five MTF results (taken in the left–right direction across the detector) acquired consecutively for a GE Senographe DS system with the edge repositioned between each acquisition. Taking the standard deviation of the spatial frequency at the 50% point of the MTF (range between 3.74 mm$^{-1}$ and 3.84 mm$^{-1}$) gave a *cov* of approximately 1%, indicating good short-term reproducibility. Longer term stability of the MTF data was assessed by examining MTF results acquired over a 17 month period for an *a*-Se unit. The *cov* for the spatial frequency of the 0.5 MTF point for five MTF results acquired over this period was 3.4% (range for the five results was 6.01 mm$^{-1}$ to 6.58 mm$^{-1}$).

Figure 2 examines the effect of geometry on the MTF. There are slight differences when comparing the edge placed directly at the detector input plane and edge placed on the breast support platform (with grid in place). With the edge on the detector, a slightly greater MTF is seen up to approximately 3 mm$^{-1}$; above 6 mm$^{-1}$; however, MTF is higher for the edge placed on the table top. Placing 4 cm PMMA at the tube port reduces MTF by a factor of
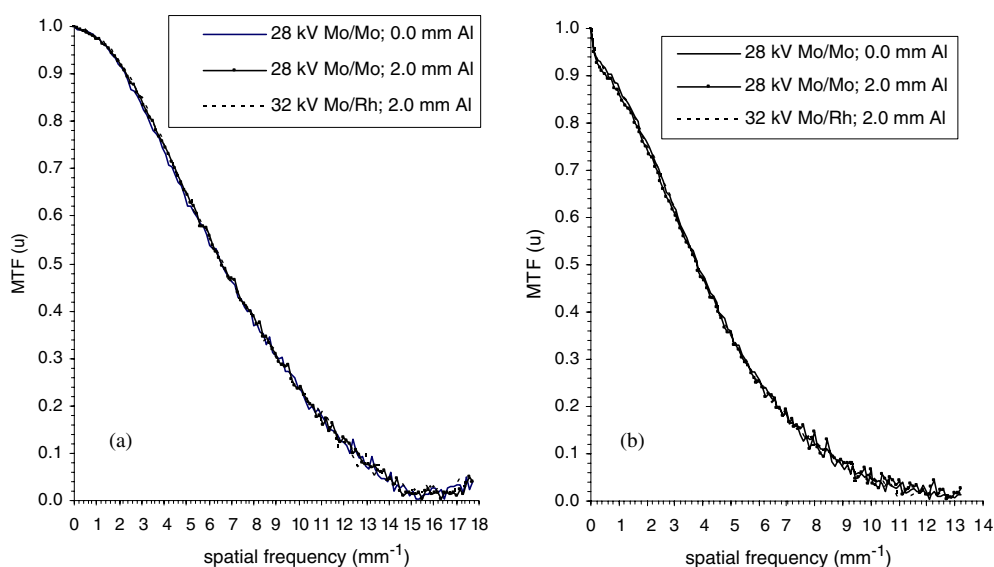
**Figure 3.** Effect of beam quality on the MTF for (a) an *a*-Se system and (b) a CsI based system (*u* direction).

approximately 0.87 (averaged up to 8 mm$^{-1}$); this is the influence of scattered radiation on the measurement.

Figure 3 plots MTF for a range of beam qualities, for *a*-Se and CsI based systems. Beam quality was changed from 28 kV Mo/Mo (no additional Al filtration) to 32 kV Mo/Rh with 2.0 mm Al filtration, representing an increase in mean energy from 16.4 keV to 21.3 keV. This is an increase in mean energy of approximately 5 keV and appears to have little effect on the MTF for both detector types.

Figure 4 shows a comparison of MTF results for similar system types; four *a*-Se units and four CsI systems. These data were acquired at 28 kV Mo/Mo with no additional filtration, the anti-scatter grid in place and the steel edge placed on the breast support platform. Only data for the *u* direction are presented in figures 4(a) and (b), as the MTFs were found to be essentially isotropic for both *a*-Se and CsI type units. Note that this is the pre-sampling MTF i.e. the MTF of the x-ray converter prior to digitization by the pixel matrix. The pre-sampling MTFs for these systems remain high at the Nyquist frequency (approximately 0.44 and 0.35 for the *a*-Se and CsI units, respectively) and therefore there may be some aliasing of signals with substantial spatial frequency content above the Nyquist frequency (Giger and Doi 1984, Dobbins 1995). The sampled MTF can be calculated if further investigation of the effect of the pixel matrix on the pre-sampled MTF is required (Dobbins 1995).

There is a reduction in the MTF of approximately 6% at the lowest spatial frequencies for the CsI type units; this is often termed the 'low-frequency drop' or LFD (Brock and Slump 1989) and is a result of long distance light scatter within the CsI phosphor. The method chosen to measure the MTF should be capable of demonstrating this reduction in modulation (Marshall 2001, Carton *et al* 2005, Samei *et al* 2006). In fluoroscopy, for example, the LFD was found in the MTF measured via the edge method for CsI based x-ray image intensifiers but was not seen with the Coltman grating method (Marshall 2001). Even edge-based MTF techniques may not show the LFD if significant low-frequency conditioning is applied to
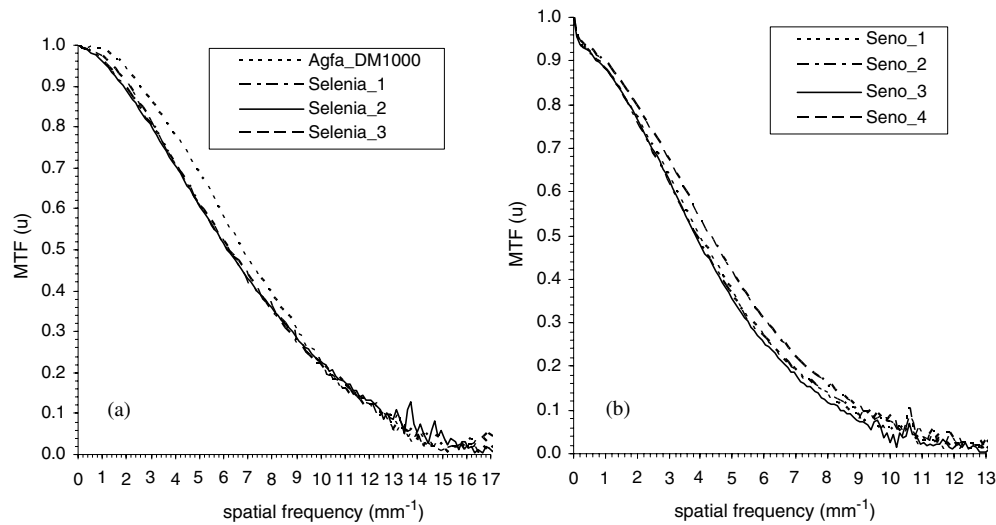
**Figure 4.** (a) MTF measured in the *u* direction (chest-wall to nipple) for four *a*-Se type units, (b) MTF results for the *u* direction for four Senographe DS systems. Results acquired at 28 kV Mo/Mo; no additional filtration; grid in; steel edge placed on the breast support platform.
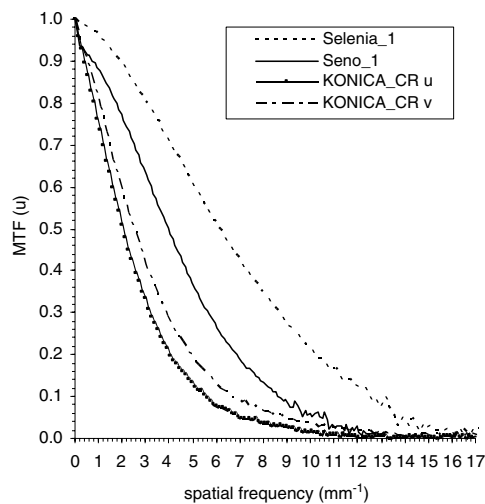


**Figure 5.** MTF results for *a*-Se (Selenia_1), CsI (Seno_1) and Konica CR systems compared.

the MTF (Carton *et al* 2005) or insufficient area around the edge is sampled for the MTF calculation (Samei *et al* 2006). Systems Seno_1, Seno_2 and Seno_3 were installed at the same time and have similar MTF results while Seno_4 is a newer system installed approximately 17 months later; MTF for this unit is approximately 10% higher averaged across all spatial frequencies.

Figure 5 compares MTF data for *a*-Se, CsI and CR based detector systems. For the Konica CR system, data are presented for both the scan direction (*u*) and subscan direction (*v*), as MTF data for CR systems are often not isotropic (Samei and Flynn 2002). The *a*-Se type

(a)        (b)
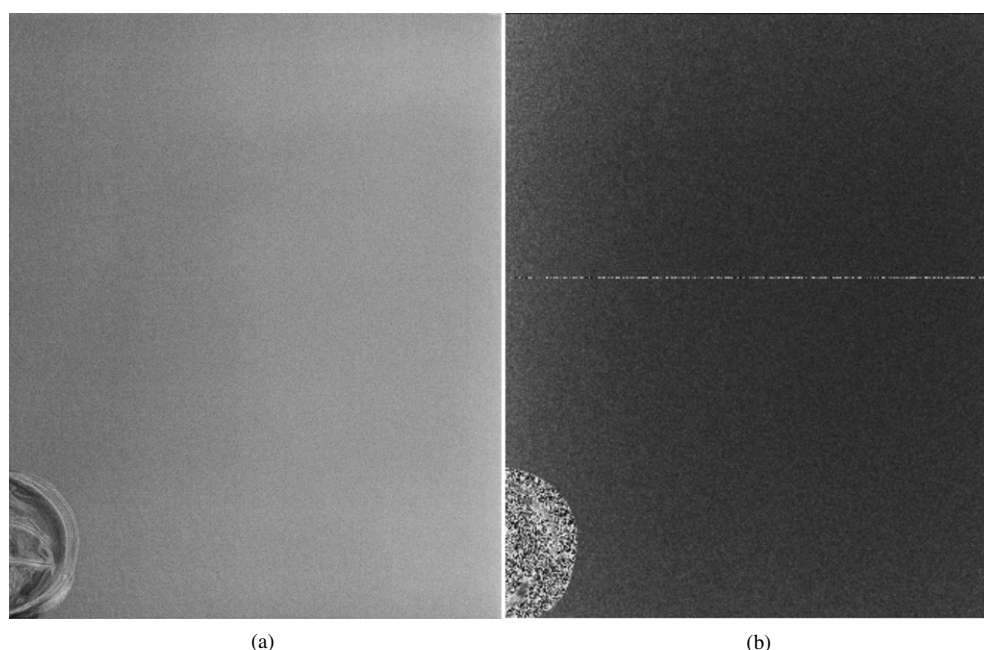
**Figure 6.** (a) Greyscale image and (b) variance image of an *a*-Se detector fault (a 10 × 10 pixel ROI was used, the chest-wall is at the right of the image). The detector was not stored according to the manufacturer's instructions.

**Table 4.** Spatial frequency for the 0.5 and 0.1 points of the MTF together with DQE at 0.2 mm$^{-1}$ and 5 mm$^{-1}$ for the various systems.

| System | Spatial frequency for 0.5 MTF (mm$^{-1}$) | Spatial frequency for 0.1 MTF (mm$^{-1}$) | DQE at 0.2 mm$^{-1}$ | DQE at 5 mm$^{-1}$ |
|---|---|---|---|---|
| Hologic Selenia | 6.15 | 12.45 | 0.55 | 0.29 |
| Agfa DM 1000 | 6.64 | 12.45 | 0.54 | 0.30 |
| GE Senographe DS | 3.95 | 8.63 | 0.46 | 0.20 |
| Konica CR | 2.01, 2.48[a] | 5.63, 6.71[a] | 0.39 | 0.08 |

[a] Scan and subscan, respectively.

units have the highest MTF of the systems assessed; spatial frequency for the 0.5 MTF point is approximately 6 mm$^{-1}$ compared to approximately 4 mm$^{-1}$ for the Senographe systems (table 4). The Konica CR system has the poorest MTF performance with the MTF reaching the 0.5 point at just 2 mm$^{-1}$. The system with the smallest pixel size actually has the lowest MTF—this is a good example of a converter limited x-ray detector system.

### 3.3. Variance image

Figure 6 shows an unusual artefact that developed within an *a*-Se based detector that was not stored according to the manufacturer's instructions. The chest-wall is at the right-hand side (RHS) in these images and a 10 × 10 pixel ROI was used; the greyscale in these images assigns white to a region of high variance and black is low variance. The greyscale image is
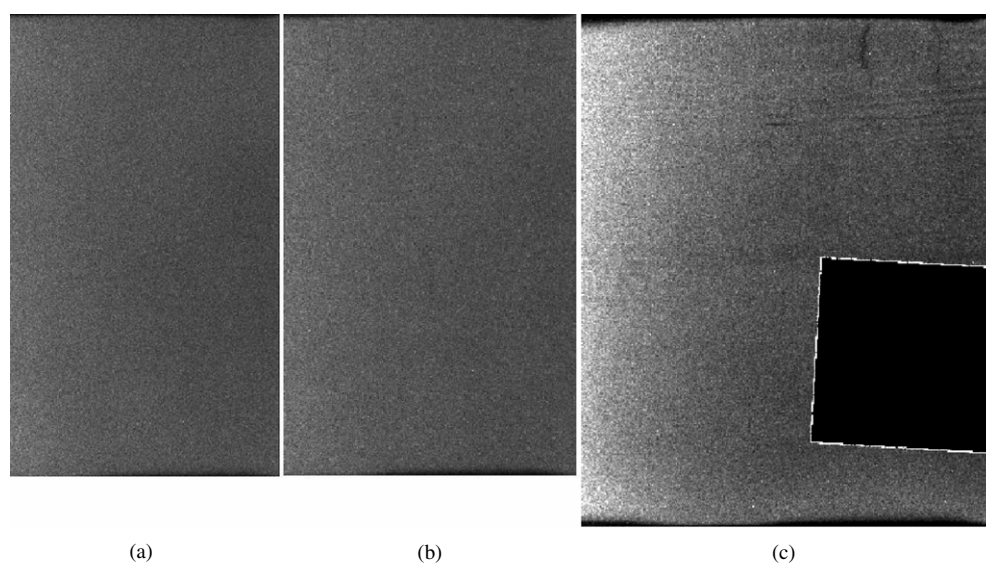
**Figure 7.** Variance images of an *a*-Se detector showing blurring at the detector edges (a $10 \times 10$ pixel ROI was used, the chest-wall is at the right of these images). Images acquired in (a) Jan-06, (b) Mar-06, (c) full image with MTF edge in Jul-06. (Note that different brightness and contrast settings were used for image (c) and this will emphasize the blurring (darker regions) at the image edge).

displayed using a high contrast setting so that the artefact is clearly seen; however, this artefact was more difficult to see at normal brightness and contrast settings (in fact it was not seen by the service engineer). The artefact is clearly visualized in the variance image; the variance image also picks out a faulty pixel line.

Figure 7 presents a series of variance images that show progressive blurring at the detector edge over a period of six months—the blurring is only slight and is seen as reduced variance i.e. two thin dark strips along the top and bottom of the image. Detailed examination of the greyscale version of the July image showed a blurring of approximately 50 pixels in length ($\sim$3.5 mm) in the $v$ direction at the detector edges. Similar problems have been reported by van Engen *et al* (2006), an effect ascribed to crystallization of the *a*-Se converter layer. Of interest is the variance image of the MTF edge image—this shows that the areas used for MTF calculation (i.e. the image centre) are some distance from the regions where the blurring occurs and underlines the value of the variance image (note that the dark region within the edge is not indicative of reduced variance but is a consequence of the equalization used for this image). Additional artefacts are seen towards the top of figure 7(c) at the RHS of the detector; this detector was replaced at this point.

### 3.4. Normalized noise power spectrum

Figure 8(a) presents NNPS results for four *a*-Se based systems acquired at an air kerma of approximately 100 $\mu$Gy at the detector (103.5 $\mu$Gy, 97.7 $\mu$Gy, 97.7 $\mu$Gy and 97.9 $\mu$Gy). As the 2D spectra are isotropic only data for the $u$ direction (chest/wall to nipple) are presented. All four sets of data have a similar form with the NNPS falling somewhat as a function of spatial frequency; there is a 30% reduction in NNPS at 0.22 mm$^{-1}$ ($\sim$3.3 $\times$ 10$^{-6}$ mm$^2$) compared to the NNPS at 6.92 mm$^{-1}$ ($\sim$2.4 $\times$ 10$^{-6}$ mm$^2$). There is a strong spike seen in the
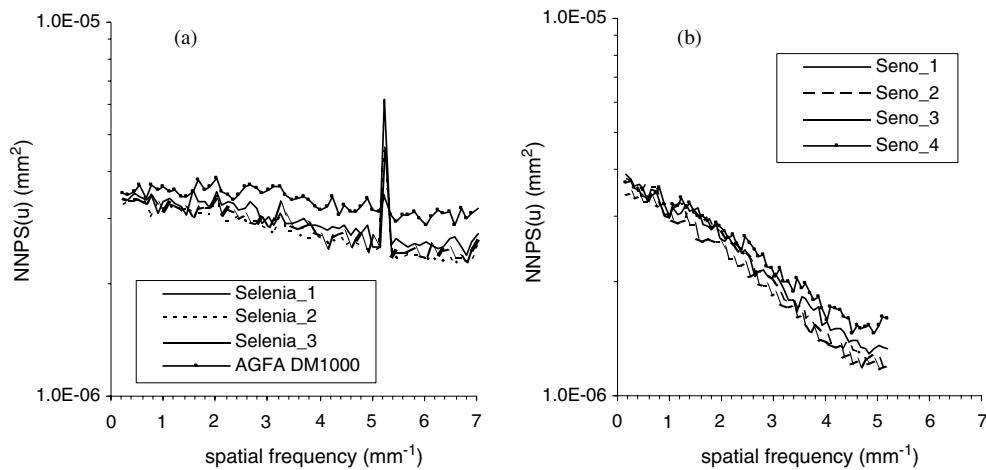
**Figure 8.** NNPS in the *u* direction measured at approximately 100 $\mu$Gy at the detector (a) *a*-Se type units and (b) GE Senographe systems.

NNPS for all four units at the same spatial frequency (5.25 mm$^{-1}$) due to periodic structures present in the image data—further spikes are seen lying off axis in figure 10(a). The four systems have the same detector cover formed out of knitted carbon fibre and this may be the cause of these features. The *cov* of the NNPS at 1 mm$^{-1}$ for these data is 7.0% (increasing to 12.3% at 5 mm$^{-1}$). Note the greater NNPS seen for the Agfa DM1000 unit; this system also has the highest MTF of the four *a*-Se units studied.

NNPS data acquired at approximately 100 $\mu$Gy (also for the *u* direction) are presented in figure 8(b) for the four GE Senographe units. Again, all four spectra have a similar shape, with a steeper reduction in NNPS with spatial frequency than is seen for the *a*-Se data. NNPS falls by 70%, from $\sim$3.7 $\times$ 10$^{-6}$ mm$^2$ at 0.16 mm$^{-1}$ to $\sim$1.3 $\times$ 10$^{-6}$ mm$^2$ at 5 mm$^{-1}$. This greater reduction in NNPS is expected due to greater correlation of the x-ray noise by the CsI x-ray converter (Rowlands and Yorkston 2000). This may be compared to the somewhat flatter NNPS seen for *a*-Se detector, which more closely resembles the white NNPS expected for the x-ray quantum noise. Comparing the NNPS results for the four Senographe units at 1 mm$^{-1}$ give a *cov* of 3.7%, which is approximately half of that found for the four *a*-Se systems. In contrast to the *a*-Se spectra, no spikes or peaks are seen in the greyscale NNPS image (figure 10(b)). This may be because the images used for the calculations were acquired with the bucky removed and therefore no carbon fibre breast support platform was present.

Figure 9 plots NNPS results for all three system types—*a*-Se, CsI and the Konica CR and emphasizes the difference in shape seen between the spectra. As with the MTF, the NNPS for the CR unit shows some anisotropy, rolling off faster in the scan direction. This is probably due to the influence of anti-aliasing filter (intended to reduce aliasing and grid line artefacts) applied along the scan direction (CEP 2006). In the subscan direction, NNPS at 11 mm$^{-1}$ compared to the NNPS at 0.18 mm$^{-1}$ has fallen by $\sim$87% (this figure is 97% for the scan direction). The sharply peaked nature of the CR NNPS is highlighted in figure 10(c); also seen are vertical and horizontal lines on the NNPS axes indicating the presence of structured noise in the image.

One of the difficulties of applying quantitative methods to a system in a clinical setting is gaining free access to the detector i.e. without the grid and detector cover. Especially difficult
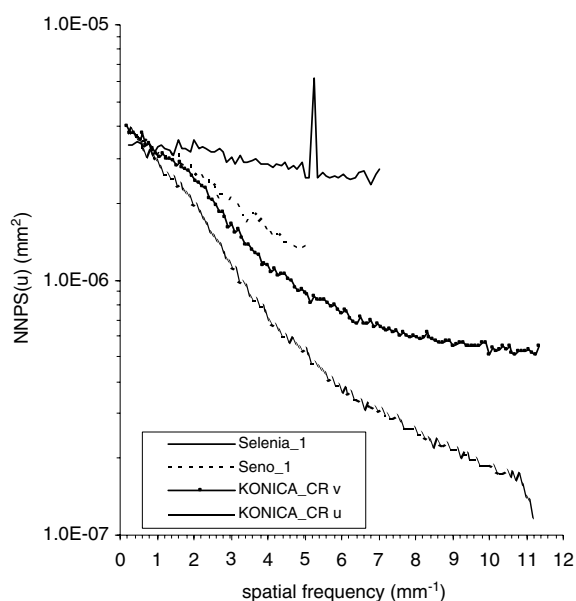
**Figure 9.** Comparison of NNPS for $a$-Se (Selenia_1), CsI (Seno_1) and Konica CR systems (approximately 100 $\mu$Gy at the detector). Data are shown just for the $u$ direction for the $a$-Se and CsI systems as NNPS for these systems is largely isotropic.



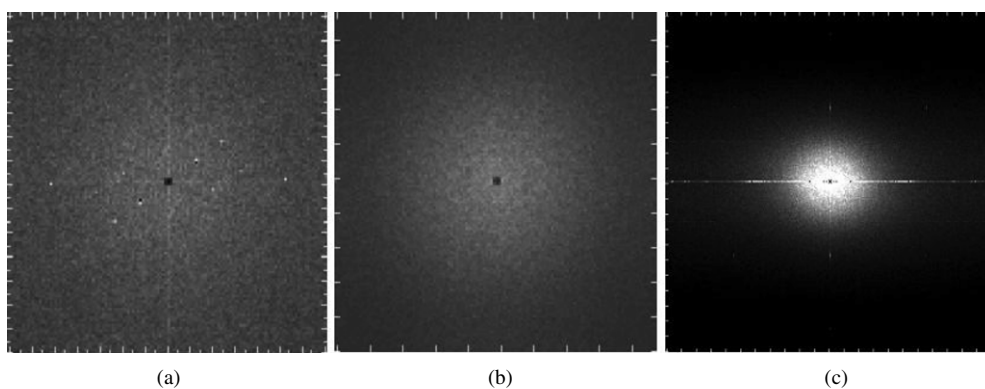**Figure 10.** NNPS for the three different detector types: (a) $a$-Se detector, (b) CsI detector, (c) CR detector (approximately 100 $\mu$Gy at the detector).

is estimating the DAK when the anti-scatter grid cannot be removed; however, if the grid could be kept in place for the measurements this would offer considerably greater protection for the detector. The effect of the grid on NNPS was investigated by acquiring flood images using an identical geometry (4 cm PMMA held at the tube exit port) but with the grid in place, for the Seno_2 unit. The grid attenuation factor measured for this geometry was 1.59 compared to a factor of 1.97 found without PMMA present. The mAs used to acquire the flood images was found by matching PV between the two cases (grid absent; grid present); the ratio between mAs values was 1.58 indicating close agreement with the measured grid factor.
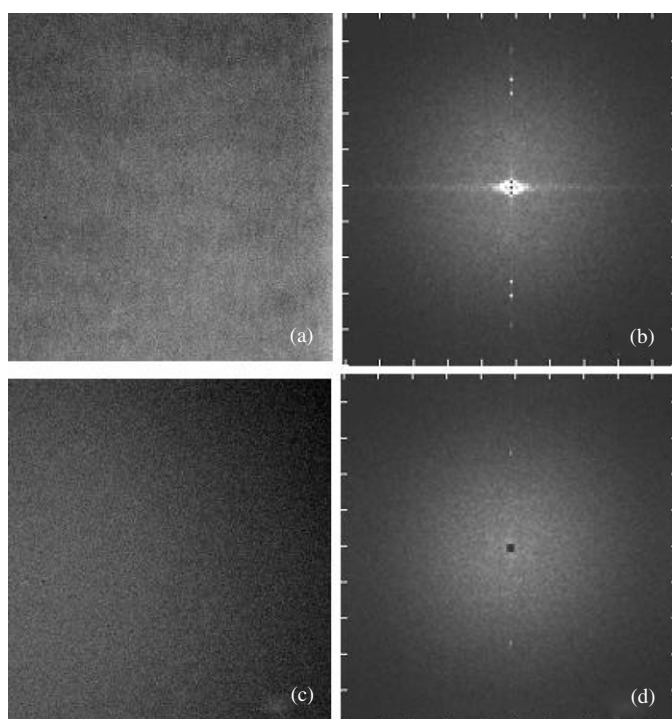
**Figure 11.** (a) Region of image acquired with anti-scatter grid in place for NNPS estimation (385 $\mu$Gy), (b) NNPS for this region, (c) the same region of image acquired without anti-scatter grid at 387 $\mu$Gy and (d) NNPS for area (c).

Figure 11(a) shows a flood image (1088 $\times$ 1088 pixels) used for NNPS estimation acquired at 385 $\mu$Gy; considerable non-uniformity can be seen across this image. The NNPS for this image is given in figure 11(b) and confirms the presence of low-frequency noise (the high NNPS value at the centre of figure 11(b)), along with increased structured noise along the NNPS axes. By way of comparison, figure 11(c) shows the same region of flood image acquired at 387 $\mu$Gy without the grid. Although there is a slow change in PV across the image, the image is more uniform. Axial structured noise is largely absent in the corresponding NNPS (figure 11(d)). Axial plots extracted from these images are given in figure 12 and indicate the elevated NNPS below $\sim$1 mm$^{-1}$. Note that the effect of the grid on the NNPS becomes less significant at lower DAK values. This is illustrated in figure 12 for NNPS data acquired at 97 $\mu$Gy; an increase in NNPS is seen below 0.5 mm$^{-1}$, however, there is little difference in NNPS at higher spatial frequencies.

Finally, stability of the NNPS (in the $u$ direction) over a period of one year was assessed for an $a$-Se unit. The *cov* for the NNPS at 1 mm$^{-1}$ is 3.6% which again is comparable to the uncertainty for a single NNPS measurement. Given the uncertainties present in the measurement set up (e.g. calibration factor, focus-chamber distance, stability of x-ray output), this is a surprisingly low figure.

### 3.5. Detective quantum efficiency

Figure 13(a) shows DQE results in the $u$ direction acquired at approximately 100 $\mu$Gy for four $a$-Se based units; similar data are plotted in figure 13(b) for the four CsI based systems (i.e.
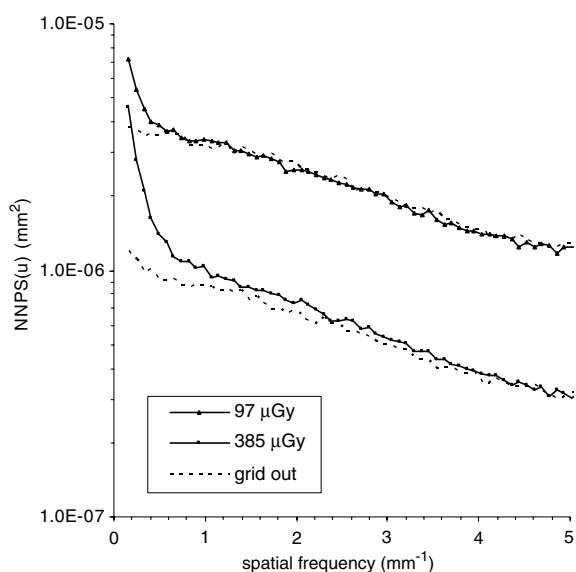
**Figure 12.** Effect of anti-scatter grid on NNPS (*u* direction) for Seno_2 measured at two different detector air kerma values. The dotted lines show NNPS measured at 97 $\mu$Gy and 387 $\mu$Gy, with the anti-scatter grid removed.
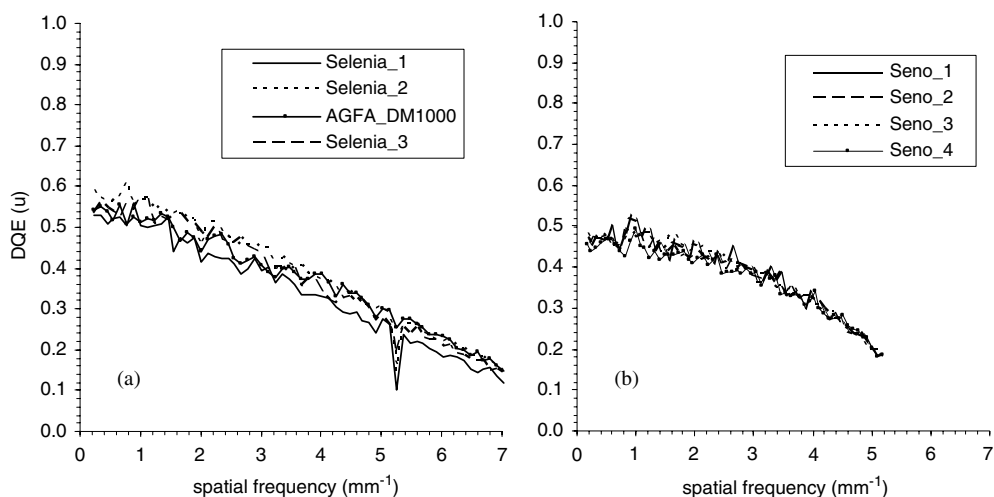


**Figure 13.** DQE for the *u* direction measured at detector air kerma of ~100 $\mu$Gy for (a) four *a*-Se based units and (b) four CsI based systems.

GE Senographe systems). Slightly greater variation is seen for the *a*-Se systems (7% *cov* at 1 mm$^{-1}$ compared to 4% *cov* for the CsI systems). It is unclear why this should be the case; however, the *a*-Se data were acquired with the carbon fibre table covering in place and this cover is subject to an additional manufacturing tolerance.

Figure 14 compares DQE for all three detector types: *a*-Se, CsI and the Konica CR plate. DQE results for both the *a*-Se and CsI are similarly shaped, while DQE of the CR system falls away more rapidly as a function of spatial frequency. This is largely the influence of
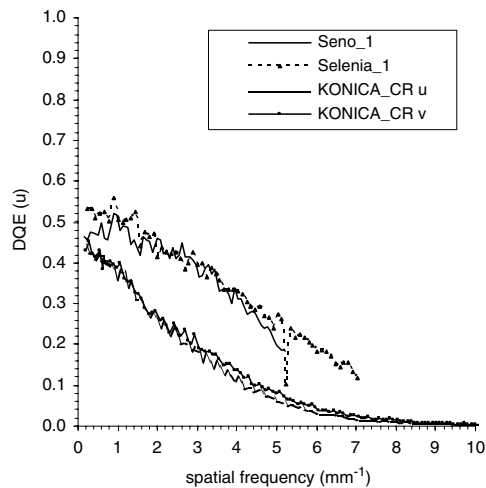
**Figure 14.** Comparison of DQE (*u* direction) measured at approximately 100 $\mu$Gy at the detector for three different detector types.

the markedly poorer MTF on the CR system DQE (figure 5). Average DQE at 0.2 mm$^{-1}$ for the *a*-Se, CsI and the Konica CR systems is 0.55, 0.46 and 0.39, respectively. Far greater difference is found at 5 mm$^{-1}$, where average DQE for the *a*-Se, CsI and Konica system is 0.28, 0.20 and 0.08, respectively (see table 4). One might therefore expect greater attenuation by the Konica system of high-frequency spatial frequency information present in the image. Note that the DQE results for the *a*-Se and CR systems were calculated without correcting for the carbon fibre cover of the breast support table or the entrance window of the CR cassette. This directly affects the DQE; for example, assuming 95% transmission for the carbon fibre cover will increase DQE by 1/0.95 i.e. by a factor 1.05.

DQE was also investigated as a function of air kerma at the detector; figure 15 presents results at target DAK values of 12.5 $\mu$Gy, 100 $\mu$Gy and 400 $\mu$Gy. Figures 15(a) and (b) give data for a Senographe and a Selenia system, respectively, while figure 15(c) plots the CR system results. Similar results are found for the integrated detector systems in figures 15(a) and (b) (i.e. the CsI and *a*-Se detectors); DQE is reduced somewhat at low DAK values. Average DQE at approximately 12.5 $\mu$Gy and 1 mm$^{-1}$ for the four Senographe units was similar at 0.38 (*cov* of 3.4%). Greater variation was found within the *a*-Se systems; DQE results at approximately 12.5 $\mu$Gy and 1 mm$^{-1}$ for the four *a*-Se units were 0.19, 0.42, 0.33 and 0.31, giving an average of 0.31 and a *cov* of 30%. The average reduction in DQE at approximately 12.5 $\mu$Gy was 33% for the *a*-Se systems, compared to the figure of 22% for the four Senographe systems. This reduction in DQE at low air kerma for both the *a*-Se and CsI detectors is probably due to electronic noise from the readout electronics (Yorker *et al* 2002). This is an additive noise source (Siewerdsen *et al* 1997, Evans *et al* 2002) and will therefore make a greater contribution to system noise at low signal (DAK) levels. The temperature of the detector in the Senographe systems is actively controlled using a pumped coolant; however, this method is not used for the *a*-Se units. It is possible that the ambient room temperature will therefore have a greater influence on the performance of the *a*-Se detectors, leading to the variation in DQE seen for the low air kerma data.

Distinctly different behaviour is observed for the CR system, where electronic noise from the photomultiplier tube readout is known to be low (Rowlands 2002). There is no reduction
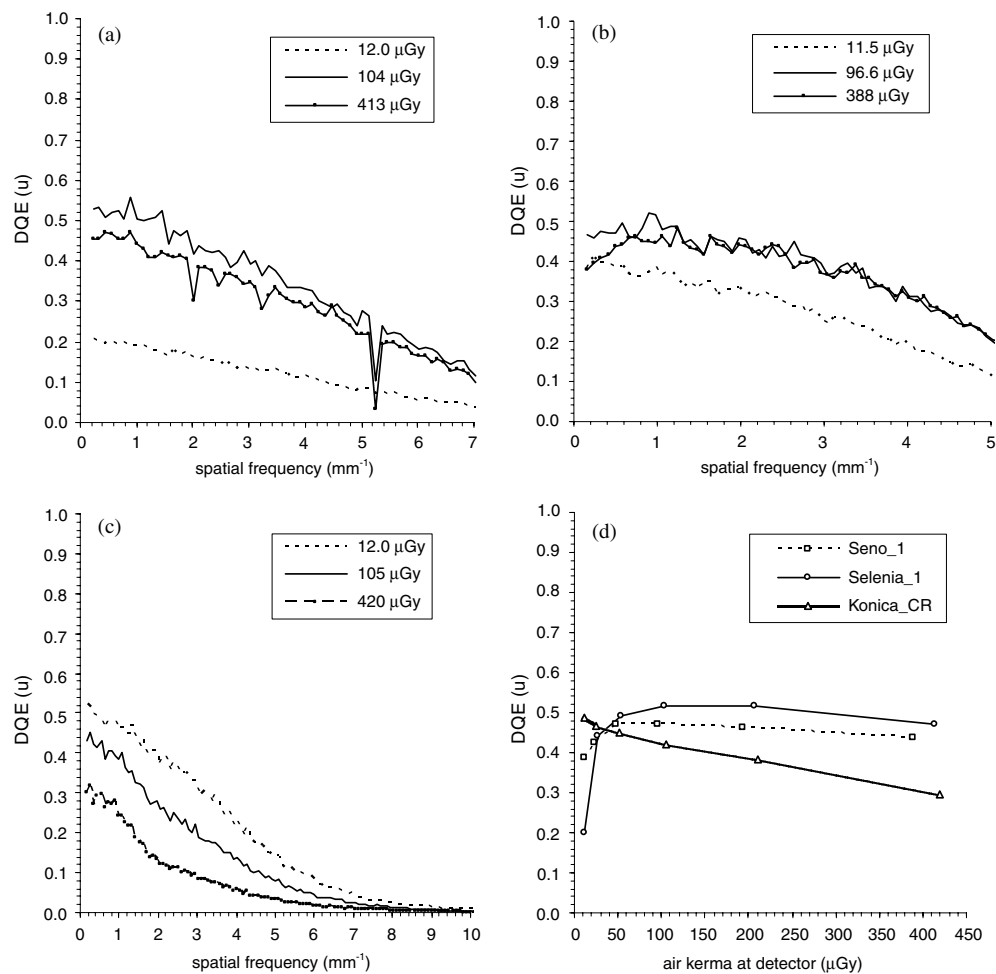
**Figure 15.** DQE ($u$ direction) measured with detector air kerma as a parameter for (a) the GE Senographe system, (b) the Hologic Selenia system and (c) the Konica CR system, and (d) DQE at 0.5 mm$^{-1}$ plotted as a function of detector air kerma.

in DQE at low air kerma; the DQE simply falls away as DAK is increased, indicating the influence of structured noise on the DQE (Illers *et al* 2004b). This is a multiplicative noise source (multiplied by the x-ray signal), which becomes progressively more important as DAK increases. There is a reduction in DQE of 40%, with the DQE falling from 0.49 at 12 $\mu$Gy to 0.30 at 420 $\mu$Gy. The trends in DQE as a function of DAK are illustrated in figure 15(d), which highlights the differences between the two integrated detectors and the CR system. The flat fielding used in integrated detector units (i.e. the application of gain correction map, spatially across the detector) will reduce the influence of structured noise on the detector DQE (Rowlands and Yorkston 2000), an effect seen at high DAK. In a previous study, it was shown that the reduction in DQE at low DAK values for an $a$-Se detector leads to a reduction in contrast resolution (Marshall 2006a) and therefore some loss of contrast resolution might be expected in dense regions of the breast for both the integrated detector systems here. The extent of this loss in contrast resolution will depend on the signal level maintained by the
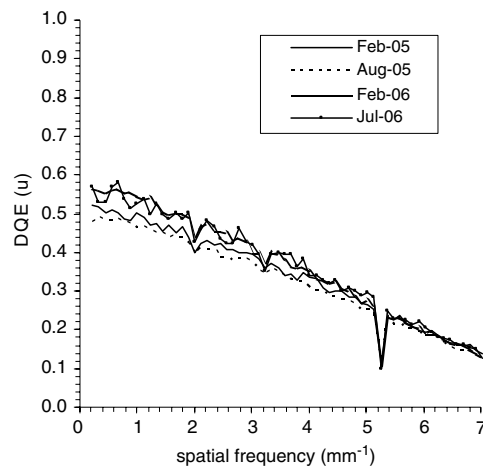
**Figure 16.** Stability of DQE (*u* direction) over a period of 17 months for an *a*-Se based system (∼100 μGy at the detector).

system in dense breast regions. This in turn would depend on the AEC design; it may be worthwhile estimating DAK for some nominal 'dense' breast sections during initial AEC testing to quantify the potential loss in contrast resolution. The CR system, while having a poorer overall DQE, does not experience this loss of DQE at low DAK levels (i.e. in the denser regions of the breast).

Finally, the stability of DQE over a period of 17 months can be examined for an *a*-Se detector. Figure 16 presents DQE data, measured in the *u* direction at approximately 100 μGy. The *cov* for the DQE at 1 mm$^{-1}$ is 6.9%, indicating reasonable stability over time. This figure is higher than the *cov* seen for the NNPS alone, which is to be expected as DQE includes uncertainties from both the NNPS and MTF data.

## 3.6. Contrast-detail results

Figure 17(a) presents the measured cd data for the three systems; these results show virtually no difference in cd performance between the two *a*-Se and CsI units while threshold contrast is somewhat higher for the Konica CR system. Averaging the ratio of threshold contrast for the CsI to *a*-Se units across all disc diameters gave a value of 0.99 (i.e. little difference); the average ratio of threshold contrast for the CR unit compared to the *a*-Se system is 1.20. The calculated data are shown in figure 17(b). Only a small difference is predicted between the CsI and *a*-Se results, echoing the trend seen for the measured cd data (the ratio of threshold contrast for the CsI system to the *a*-Se system is 0.95). The calculations indicate an increase in threshold contrast for the CR system compared to the integrated detector systems, again following the measured cd data. There is some detail diameter dependence: the ratio of threshold contrast for the CR system to that for the *a*-Se system rises from 1.08 for 0.4 mm diameter discs to 1.40 for 0.1 mm discs (average across all disc diameters is 1.14).

To some extent, these results follow the DQE results presented in figure 14; the *a*-Se and CsI have a similar DQE up to 5 mm$^{-1}$ (although a factor to allow for table cover transmission for the *a*-Se system should be included) and little difference is seen in the cd results. The reduced DQE for the CR system translates into a poorer cd result compared to the integrated detector systems, although strong differences in DQE are clearly reduced when translated into
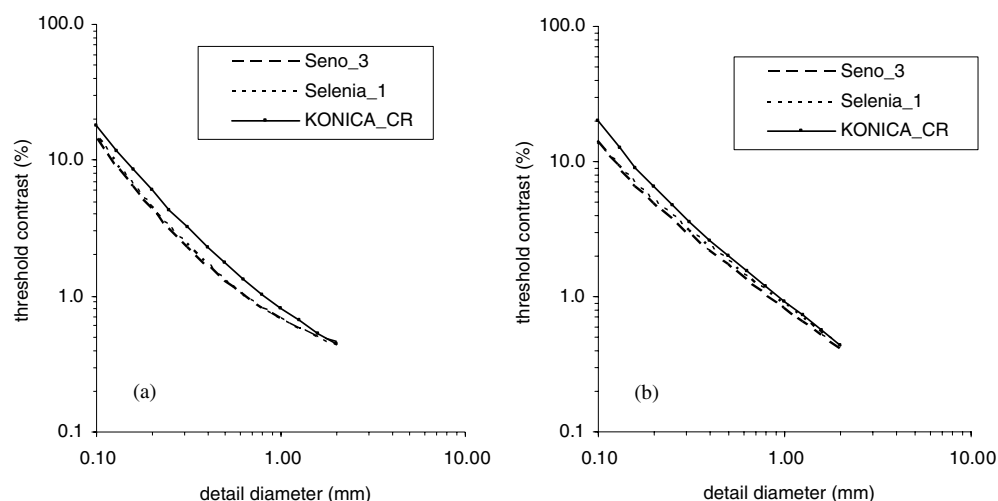
**Figure 17.** (a) Threshold contrast-detail results for one observer reading two images (28 kV Mo/Mo and ~100 $\mu$Gy at the detector) for a GE Senographe system (Seno_3), a Hologic Selenia system (Selenia_1) and for a Konica CR system, (b) threshold contrast for these three systems was calculated using a matched filter observer for the $u$ direction.
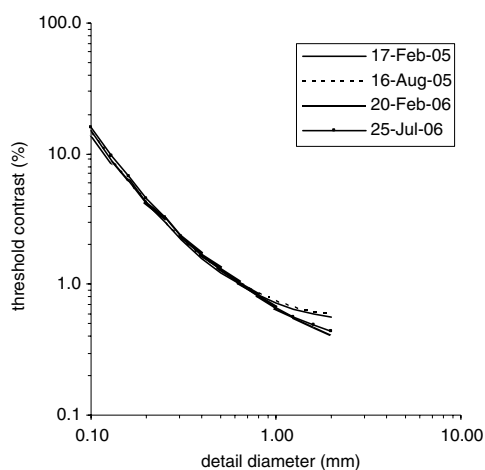


**Figure 18.** Stability of cd results over a 17 month period for an $a$-Se system (Selenia_1). The *cov* averaged over all detail sizes (0.1 mm to 2 mm) is 6%. Acquisition factors were 28 kV, Mo/Mo and approximately 100 $\mu$Gy at the detector.

cd performance. Note that while these data give some insight into the relative cd behaviour between these units, calculation of absolute cd results for comparison against some external performance scale such as the EUREF acceptable curve remains a problem. One option might be to calculate threshold contrast for some standard observer model for both a typical S/F system (which would equate to the minimum performance standard) and for the digital detector under investigation.

Finally, cd performance of an $a$-Se unit (Selenia_1) can be examined over time and compared against the DQE data. Figure 18 plots cd data over a 17 month period for this unit;

a second-order polynomial curve has been fitted to the data to smooth the results. Acquisition factors were 28 kV, Mo/Mo and approximately 100 $\mu$Gy at the detector. The *cov* averaged over all detail sizes (0.1 mm–2 mm) is 6%; this is similar to the *cov* found for the DQE data given in figure 16 (*cov* $\approx$ 7%). If detector DQE is stable over time then this should result in stable cd results and this appears to be the case here.

## 4. Conclusions

This study has described initial implementation of objective image parameters as part of a routine QA programme for FFDM systems. Assuming that detector response (i.e. the STP) is being measured routinely, calculation of these parameters requires the acquisition of just one further (edge) image, from which the MTF is calculated. Once the images have been saved to the network or stored on some portable medium, the transfer, calculation and storage of results in a database takes approximately 20 min.

The acquisition of these parameters has been shown to have good short- and long-term reproducibility; essential properties if a method is to be suitable for use in a QA programme. Variance images are a sensitive means of quickly and easily assessing the entire image for faults such as detector artefacts and directional blurring. Following this, the NNPS can be calculated routinely from just one flood image acquired at some nominal target DAK (for example 100 $\mu$Gy). Ideally, the flood images needed for NNPS calculation should be acquired with the antiscatter grid removed as the presence of the grid can increase low spatial frequency noise, especially at high DAK values. Removal of the grid is essential if an accurate estimate of detector DAK is required for the DQE measurement. A limitation of this method is the presence of detector covers of unknown composition and thickness on these systems; this currently limits the accuracy of the DQE estimate. However, given the quality and depth of information gained with regard to overall x-ray detector performance through the use of quantitative measurements, the additional time spent in the acquisition and calculation of these data is certainly worthwhile and their inclusion as part of a routine QA programme is recommended.

## Acknowledgments

## References

Aufrichtig R 1999 Comparison of low contrast detectability between a digital amorphous silicon and a screen–film based imaging system for thoracic radiography *Med. Phys.* **26** 1349–58
Aufrichtig R and Xue P 2000 Dose efficiency and low-contrast detectability of an amorphous silicon x-ray detector for digital radiography *Phys. Med. Biol.* **45** 2653–69
Bloomquist A K *et al* 2006 Quality control for digital mammography in the ACRIN DMIST trial: part I *Med. Phys.* **33** 719–36
Borasi G, Samei E, Bertolini M, Nitrosi A and Tassoni D 2006 Contrast-detail analysis of three flat panel detectors for digital radiography *Med. Phys.* **33** 1707–19
Brock M and Slump C H 1989 Automatic determination of image quality parameters in digital radiographic imaging systems *Proc. SPIE* **1090** 246–56
Carton A K, Vandenbroucke D, Struye L, Maidment A D, Kao Y H, Albert M, Bosmans H and Marchal G 2005 Validation of MTF measurement for digital mammography quality control *Med. Phys.* **32** 1684–95

CEP (Centre for Evidence-based Purchasing) 2006 Computed Radiography (CR) Systems for General Radiography: a Comparative Report *Report 06033* 2nd edn, ed I D Honey *et al* (London, UK: Centre for Evidence-based Purchasing)

Cunningham I A and Reid B K 1992 Signal and noise in modulation transfer function determinations using slit, wire and edge techniques *Med. Phys.* **19** 1037–44

Dobbins J T III 1995 Effects of undersampling on the proper interpretation of modulation transfer function, noise power spectra, and noise equivalent quanta of digital imaging systems *Med. Phys.* **22** 171–81

Dobbins J T III 2000 Image quality metrics for digital systems *Physics and Psychophysics Vol 1 of Handbook of Medical Imaging* ed J Beutel, H L Kundel and R L Van Metter (Bellingham: SPIE) pp 161–222

Dobbins J T III, Samei E, Ranger N T and Chen Y 2006 Intercomparison of methods for image quality characterization: II. Noise power spectrum *Med. Phys.* **33** 1466–75

EC (European Commission) 2006 *European Guidelines for Quality Assurance in Breast Cancer Screening and Diagnosis* 4th edn (Brussels: European Commission)

Evans D S, Workman A and Payne M 2002 A comparison of the imaging properties of CCD-based devices used for small field digital mammography *Phys. Med. Biol.* **47** 117–35

Giger M L and Doi K 1984 Investigation of basic imaging properties in digital radiography: 1. Modulation transfer function *Med. Phys.* **11** 287–94

Hay G A, Clarke O F, Coleman N J and Cowen A R 1985 A set of x-ray test objects for quality control in television fluoroscopy *Br. J. Radiol.* **58** 335–44

IEC (International Electrotechnical Commission) 2004 Medical electrical equipment—characteristics of digital x-ray imaging devices: Part 1. Determination of the detective quantum efficiency *IEC 62220-1* (Geneva: International Electrotechnical Commission)

Illers H, Buhr E, Bergmann D and Hoeschen C 2004a Measurement of the detective quantum efficiency (DQE) of digital x-ray imaging devices according to the standard IEC 62220-1 *Proc. SPIE* **5368** 177–87

Illers H, Vandenbroucke D and Buhr E 2004b Measurement of correlated noise in images of computed radiography systems and its influence on the detective quantum efficiency *Proc. SPIE* **5368** 639–47

IPEM 2005a Commissioning and Routine Testing of Mammographic X-Ray Systems *Report 89* ed A C Moore, D R Dance, D S Evans, C P Lawinski, E M Pitcher, A Rust and K C Young (New York: IPEM)

IPEM 2005b Recommended Standards for the Routine Performance Testing of Diagnostic X-Ray Imaging Systems *Report 91* ed P Hiles, A Mackenzie, A Scally and B Wall (New York: IPEM)

Maidment A D A, Albert M, Bunch P C, Cunningham I A, Dobbins J T III, Gagne R M, Nishikawa R M, Wagner R F and Van Metter R L 2003 Standardization of NPS measurement: interim report of AAPM TG16 *Proc. SPIE* **5030** 523–32

Marshall N W 2001 The practical application of signal detection theory to image quality assessment in x-ray image intensifier-TV fluoroscopy *Phys. Med. Biol.* **46** 1631–49

Marshall N W 2006a A comparison between objective and subjective image quality measurements for a full field digital mammography system *Phys. Med. Biol.* **51** 2441–63

Marshall N W 2006b Retrospective analysis of a detector fault for a full field digital mammography system *Phys. Med. Biol.* **51** 5655–73

Metz C E, Wagner R F, Doi K, Brown D G, Nishikawa R M and Myers K J 1995 Toward consensus on quantitative assessment of medical imaging systems *Med. Phys.* **22** 1057–61

NHSBSP (National Health Service Breast Screening Programme) 2006 Commissioning and Routine Testing of Full Field Digital Mammography Systems NHSBSP Equipment *Report 0604* (Sheffield: NHSBSP Publications)

Rowlands J A 2002 The physics of computed radiography *Phys. Med. Biol.* **47** R123–66

Rowlands J A and Yorkston J 2000 Flat panel detectors for digital radiography *Physics and Psychophysics Vol 1 of Handbook of Medical Imaging* ed J Beutel, H L Kundel and R L Van Metter (Bellingham: SPIE) pp 223–328

Samei E and Flynn M J 2002 An experimental comparison of detector performance for computed radiography systems *Med. Phys.* **29** 447–59

Samei E and Flynn M J 2003 An experimental comparison of detector performance for direct and indirect digital radiography systems *Med. Phys.* **30** 608–22

Samei E, Flynn M J and Reimann D A 1998 A method for measuring the presampled MTF of digital radiographic systems using an edge test device *Med. Phys.* **25** 102–13

Samei E, Ranger N T, Dobbins J T III and Chen Y 2006 Intercomparison of methods for image quality characterization: I. Modulation transfer function *Med. Phys.* **33** 1454–65

Siewerdsen J H, Antonuk L E, el-Mohri Y, Yorkston J, Huang W, Boudry J M and Cunningham I A 1997 Empirical and theoretical investigation of the noise performance of indirect detection, active matrix flat-panel imagers (AMFPIs) for diagnostic radiology *Med. Phys.* **24** 71–89

Tapiovaara M J 1993 SNR and noise measurements for medical imaging: II. Application to fluoroscopic x-ray equipment *Phys. Med. Biol.* **38** 1761–88

van Engen R E, Swinkels L J, Oostveen T D, Geertse T D and Visser R 2006 Using a homogeneity test as weekly quality control on digital mammography units *Proc. 8th Int. Workshop on Digital Mammography LNCS* vol 4046 ed S M Astley, M Brady, C Rose and R Zwiggelarr (Berlin: Springer)

Wagner R F and Brown D G 1985 Unified SNR analysis of medical imaging systems *Phys. Med. Biol.* **30** 489–518

Workman A and Cowen A R 1993 Signal, noise and SNR transfer properties of computed radiography *Phys. Med. Biol.* **38** 1789–1808

Yaffe M J *et al* 2006 Quality control for digital mammography: Part II recommendations from the ACRIN DMIST trial *Med. Phys.* **33** 737–52

Yorker J G, Jeromin L S, Lee D L Y, Palecki E F, Golden K P and Jing Z 2002 Characterization of a full field digital mammography detector based on direct x-ray conversion in selenium *Proc. SPIE* **4682** 21–9